scientific reports

Check for updates

OPEN

Characterizing bone density pattern and porosity in the human ossicular chain using synchrotron microtomography

Aleksandra Ivanovic[1,2,3✉], Fabian Schalbetter[1], Margaux Schmeltz[3], Wilhelm Wimmer[1,4], Marco Caversaccio[1,2], Marco Stampanoni[3,5], Anne Bonnin[3] & Lukas Anschuetz[1,6,7]

The auditory ossicles amplify and transmit sound from the environment to the inner ear. The distribution of bone mineral density is crucial for the proper functioning of sound transmission as the ossicles are suspended in an air-filled chamber. However, little is known about the distribution of bone mineral density along the human ossicular chain and within individual ossicles. To investigate this, we analyzed fresh-frozen human specimens using synchrotron-based phase-contrast microtomography. In addition, we analyzed the volume and porosity of the ossicles. The porosity for the auditory ossicles lies, on average, between 1.92% and 9.85%. The average volume for the mallei is 13.85 ± 2.15 mm^3, for the incudes 17.62 ± 4.05 mm^3 and 1.24 ± 0.29 mm^3 for the stapedes. The bone density distribution showed a similar pattern through all samples. In particular, we found high bone mineralization spots on the anterior crus of the stapes, its footplate, and along areas that are crucial for the transmission of sound. We could also see a correlation between low bone mineral density and holey areas where the bone is only very thin or missing. Our study identified a similar pattern of bone density distribution within all samples: regions exposed to lower forces generally show higher bone density. Further, we observed that the stapes shows high bone mineral density along the anterior crus and its footplate, which may indicate its importance in transmitting sound waves to the inner ear.

The human middle ear is a small, air-filled chamber between the outer and the inner ear. It holds three tiny bones, the auditory ossicles, which transmit sound vibrations from the environment to the inner ear. The ossicles consist of malleus, incus, and stapes and are arranged in a chain-like configuration, with the malleus attached to the eardrum and the stapes attached to the inner ear via the oval window, as indicated in Fig. 1. The morphology of the middle ear, including the shape and size of the ossicles, has been studied since the nineteenth century[1] and is critical for its primary function—sound transmission. An essential part of the morphology of the ossicular chain is the distribution of bone density within the ossicles. Density affects their stiffness and mass, which in turn affects their ability to transmit sound. Unlike long bones, human auditory bones complete ossification shortly after birth, and little ossicular bone remodeling has been observed after that[2–5]. Recent studies have shown that the overall mineralization is much higher than in long bones[3] and that the density distribution within the ossicles is not uniform[6]. It has also been hypothesized that there is a variable degree of bone remodeling due to the different loads in this tiny biomechanical system[4,6].

Hill et al. suggest that bone remodeling should not occur at sites of ligamentous attachment in order to provide stability[8]. Thus, these sites are expected to have higher bone mineralization. The stapes footplate, which is in contact with the inner ear, has been found to have a higher density than other parts of the ossicles[4]. It is considered essential for effective sound transmission, as the higher density of the footplate allows an efficient coupling with the fluid in the inner ear. Otherwise, little is known about the distribution of bone density along

[1]Department of Otorhinolaryngology, Head and Neck Surgery, Inselspital, Bern University Hospital, Universityof Bern, Bern, Switzerland. [2]Hearing Research Laboratory, ARTORG Center for Biomedical Engineering Research, University of Bern, Bern, Switzerland. [3]Paul Scherrer Institut, Swiss Light Source, Villigen PSI, Villigen, Switzerland. [4]Department of Otorhinolaryngology, Technical University of Munich, TUM School of Medicine, Klinikum rechts der Isar, Munich, Germany. [5]Institute for Biomedical Engineering, University and ETH Zürich, Zurich, Switzerland. [6]Department of Otorhinolaryngology, Head and Neck Surgery, CHUV Centre Hospitalier Universitaire Vaudois and University of Lausanne, Lausanne, Switzerland. [7]The Sense Innovation and Research Center, Lausanne and Sion, Switzerland. ✉email: aleksandra.ivanovic@unibe.ch
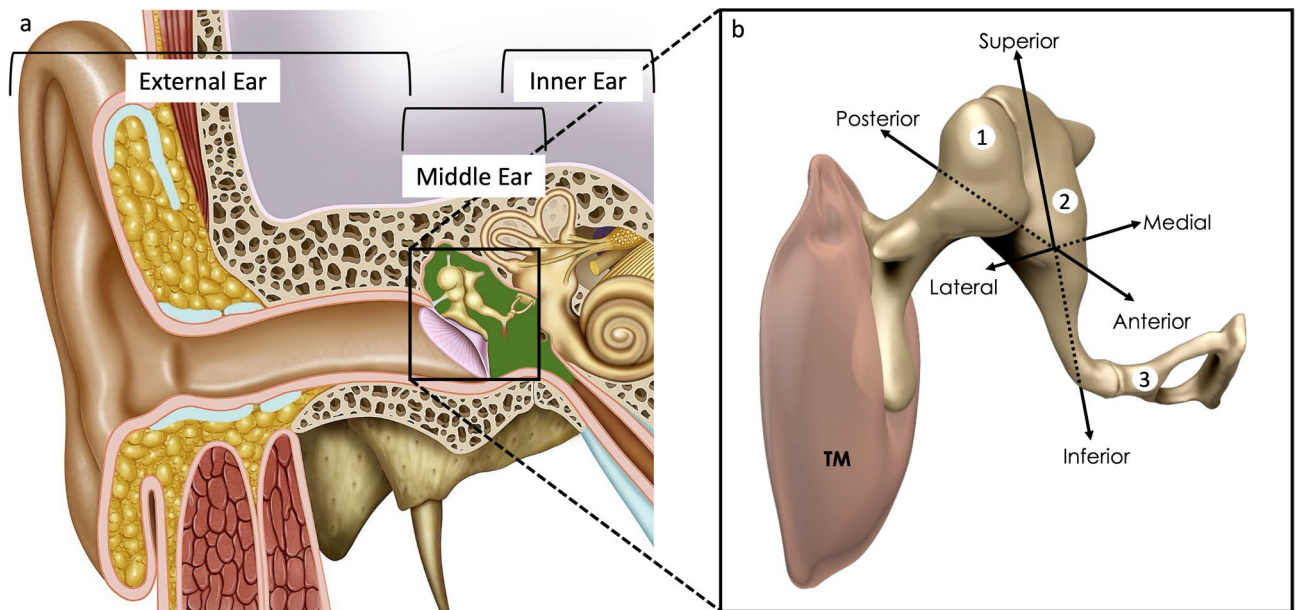
Figure 1. Sagittal cut through a right human ear. The three compartments of the human ear are indicated in (**a**). The zoom-in to the middle ear in (**b**) shows the tympanic membrane (TM), the malleus (1) attached to it, the incus (2), and the stapes (3) in their chain-like configuration. Adapted from[7] and "Radiopaedia—Drawing Middle ear ossicles and tympanic membrane—no labels" at AnatomyTOOL.org by Frank Gaillard, license: Creative Commons Attribution-NonCommercial-NoDerivs.

the human ossicular chain and within individual ossicles. Nevertheless, the mineralization pattern of the ossicles appears to be critical for the proper functioning of sound transmission[2–5,9]. A decreased bone density, as observed in osteogenesis imperfecta (OI), which is also associated with a thickened and fixed stapes footplate, often leads to conductive (and later mixed) hearing loss[10]. In 1998, Marotti et al.[11] investigated osteocyte lacunae in auditory ossicles and clavicles. Osteocytes are essential for maintaining the dynamic nature of bone and its various functions. They are recognized as the primary sensors of mechanical stress on the bone, controlling its formation and resorption by releasing soluble factors[12–14]. Additionally, they oversee mineral deposition and chemistry within the bone matrix. He found that the process of osteocyte degeneration in auditory ossicles is very rapid; over 40% of the cells die within the first two years, while in other bones, the values are around 1% at the same age and reach 40% in older adults. Further, he found a positive correlation between osteocyte death and the distance from vascular channels. He further hypothesized that this abrupt phenomenon of osteocyte death shortly after birth, which leads to the loss of their ability to react to stain and stress, allows them to achieve the structural stability they need to perform the transmission of sound.

The morphology of the auditory ossicles is most frequently studied using two techniques: micro-computed tomography (µCT)[15–18] and histological analysis[19–22]. µCT allows researchers to visualize the internal structure of the ossicles in three dimensions. However, with an isotropic voxel size reported between 10 µm to 80 µm, one cannot differentiate smaller areas within the ossicles. Therefore, histological analysis has been the gold standard technique for morphological analysis. Nevertheless, here, we only look at 2D slices, and it requires sectioning of decalcified tissue, which leads to sample destruction and deformation. Further, decalcification makes studying bone mineralization patterns within the ossicles impossible. An emerging technique to study the ear is synchrotron-based X-ray phase-contrast microtomography, which allows an increase in the resolution compared to µm CT without prior staining or destroying the sample. Additionally, phase contrast imaging provides more information about the sample due to increased contrast. The highest voxel size reported to study human middle ear ossicles so far was 0.65 µm, reported by Anschuetz et al.[6]. Therefore, this innovative approach appears particularly suitable to study the mineralization properties of the ossicular chain.

We aim to investigate the bone density distribution in the in-situ human ossicular chain using synchrotron-based phase-contrast microtomography and analyze the volume and porosity of the single ossicles. To the best of our knowledge, a porosity analysis of human middle ear ossicles has yet to be reported. Understanding the bone density patterns within the ossicles is essential for investigating middle ear biomechanics and advancing future translational and clinical applications.

Results

Volume and porosity analysis

Table 1 presents the volume (in mm³) and porosity (in %) for the three auditory ossicles and the three samples. The average volumes are 13.85 ± 2.15 mm³ for the mallei, 17.62 ± 4.05 mm³ for the incudes, and 1.24 ± 0.29 mm³ for the stapedes. The average porosity of the ossicles ranges from 1.92 to 9.85%, with the mallei being the most compact and the stapedes the least compact. Sample 1 has the smallest overall ossicle volumes compared to the

	Sample 1	Sample 2	Sample 3	Average	Literature
Malleus					
Volume [mm³] Porosity [%]	11.38 2.38	14.79 1.38	15.38 2.02	**13.85 ± 2.15** **1.92 ± 0.41**	12.7 ± 2.0 /
Incus					
Volume[mm³] Porosity[%]	13.78 2.94	17.82 4.14	21.89 4.59	**17.62 ± 4.05** **3.89 ± 0.69**	14.8 ± 2.5 /
Stapes					
Volume[mm³] Porosity[%]	0.95 9.77	1.54 7.32	1.25 12.46	**1.24 ± 0.29** **9.85 ± 2.10**	1.43 ± 0.24 /

Table 1. Volume and porosity measurements. The values are indicated for all ossicles of the three samples scanned. The average value and standard deviation are in bold, and in comparison, the reported values and standard deviations from previous literature[23]. The average values lay within previous reports.

other samples. Sample 3 has the largest volumes for the malleus and incus, and sample 2 has the largest volume for the stapes.

The differences in the volume of the three ossicles between the samples can be visualized with 3D volume representations of the ossicles, as shown in Fig. 2. The differences in volume in the incudes are particularly clear, as the volume differences are the biggest. We observed that the incus in sample 3 is the longest and widest, which accounts for its largest volume. This positive correlation between length, width, and volume is also evident in the incudes of samples 1 and 2. Similarly, the malleus in all three samples has a consistent positive relationship
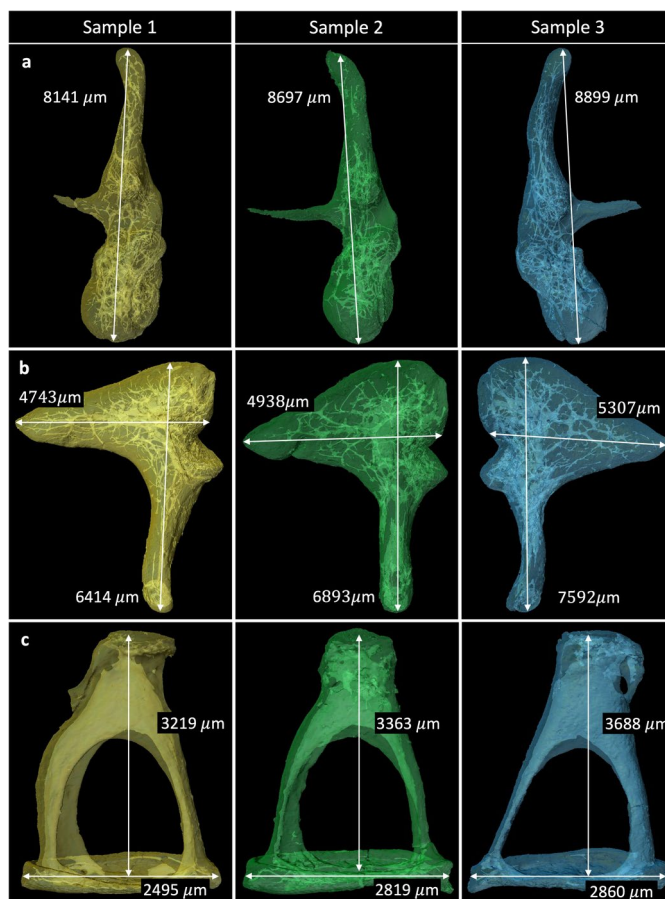

Figure 2. Semi-transparent 3D surface renderings of the three ossicles from the three samples, view from superior. The first column shows the ossicles of sample 1, displayed in yellow. In the middle column, the ossicles of sample 2 are shown in green, and in the last column, in blue, the ossicles of sample 3. The white double arrows indicate the ossicles' length and width. The first row (**a**) shows the three mallei, the second row, (**b**) shows the incudes, and the last row, (**c**) shows the stapedes. The overall size of the ossicles increases from sample 1, shown in yellow, to sample 2, shown in green, to sample 3, in blue.

between length, width, and volume. However, the stapedes exhibit a different pattern. Despite the stapes in sample 3 being the longest, sample 2 has the largest stapes volume because its stapes head is the least hollow, leading to a greater overall volume.

Further, we can virtually cut along the long process of the incus to visualize different parts and compare the structure of the three samples, shown in Fig. 3. The right panel shows the porosity calculations of three different regions of interest (ROIs) along the incus, the body (1), the long process (2), and the lenticular process (3). The largest intra-sample differences are observed between the body and the lenticular process, while the largest inter-sample differences are found along the long process of the incus. Sample 1 is much more compact compared to samples 2 and 3. In sample 2, substantial portions of bone are missing along the lenticular process (indicated with an asterisk), whereas samples 1 and 3 retain more bone in this area. Additionally, sample 3 has more hollow areas along the long process of the incus compared to the other two samples. Moreover, we observe a distinct color difference between (a), (b), and (c), representing the bone mineral density. However, towards the periphery of the incus body, all samples show an increase in bone density (indicated with little arrows). We can see a similar dense lining along the ossicle for all samples.

We visually examined the vasculature in the 3D renderings. Based on the classification of vessels provided by Manoharan et al.[24], samples 1 and 2 appear to have a normal range of vascular channels. In contrast, sample 3 has a below-average number of vessels.
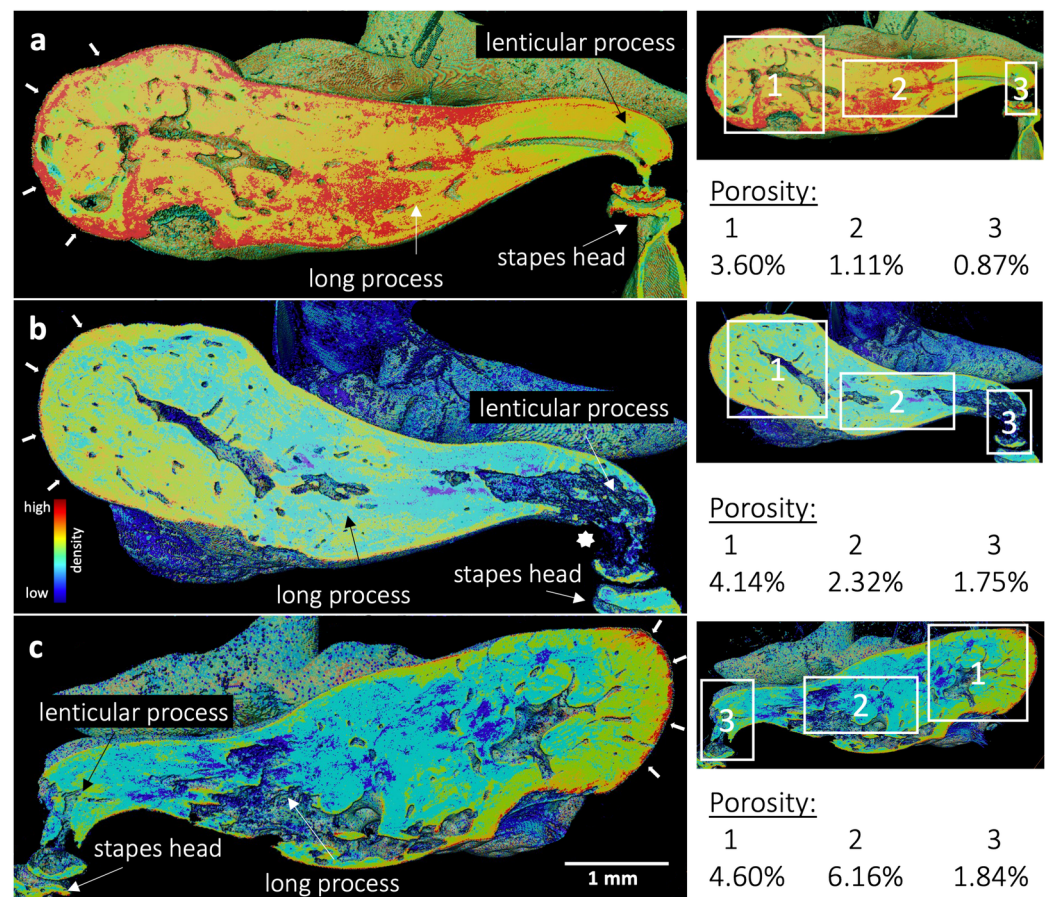

Figure 3. Sagittal cut through the bodies of the three incudes. On the left panel, (**a**) shows the cavities in incus 1. The bone appears compact; only the main vascular channels are visible. The sample appears dense with several lower mineralized spots (color-coded in red and orange or turquoise, respectively). The incus of sample 2 is displayed in (**b**), revealing a larger central cavity in the incus body and prominently more hollowed space along the long process towards the lenticular process, marked with an asterisk. In (**c**), the incus of sample 3 is displayed. Here, we can see an even more prominent central cavity in the body and a transition to the long process, which is substantially more hollow. In this area, we cannot differentiate any blood vessels. The body appears turquoise and dark blue, indicating the lowest bone density of the three incudes. Sample 1 (**a**) shows the highest mineral bone density in the range of 140–170. Sample 2 (**b**) is in a medium bone density range between 120 and 150. Sample 3 is the least dense, in the range of 110–130. Towards the periphery of the incus body, all samples show an increase in bone density, indicated with little arrows. On the right panel, three ROIs are indicated with a square and a number. Their corresponding porosity is noted.

Bone density distribution

Based on color-coded segmentations of the ossicular chain, we analyzed bone density distributions using 3D volume renderings. The colormap, based on the scale we defined in *Methods*, goes from dark blue, representing the least dense areas, starting at 110, to dark red, representing the most dense range up to 170 (see Fig. 9).

An Amira built-in module called *Clipping Plane* allowed us to cut through the 3D volume rendering and display any plane. A similar pattern of high bone density around low-force regions is observed in all samples: In the periphery of the malleus and incus around the incudomalleolar joint (IMJ) and along the lateral side of the long process. Moreover, the anterior crus and parts of the stapes footplate also show high-density spots. Sample 1 shows the highest overall bone density, with values ranging from 120 to 170, illustrated in Fig. 4. In contrast, Samples 2 and 3 show more low-density areas, with values ranging from 110 to 160, illustrated in Figs. 5 and 6, respectively.

In addition, the attachment site of the stapedial muscle at the neck of the stapes was analyzed in detail and shown in Fig. 7. Overall, there is a large variability in bone mineral density between the three samples. However, they all show high density at the insertion site of the stapedial muscle, the anterior crus, and along the stapes footplate.

Discussion

Here, for the first time, we report the analysis of the volume, porosity, and bone density distribution within the ossicular chain of fresh-frozen human temporal bones.

We have found that the degree of porosity and bone density within the same area appears to have a negative correlation. The incus emerges as the most spongy ossicle and the least mineralized. In addition to the similar pattern of high-density regions along areas of low force, we also found areas of high density at the attachment of the stapedius muscle and the stapes footplate in all samples. In contrast to the malleus and the incus, the stapes is a hollow ossicle, which explains the higher degree of overall porosity.

Our observations regarding the volume analysis lay, on average, within the standard deviation of previously reported values 23 (see Table 1). Despite the small sample size, we observed a high anatomical variability in our study. While it is well established that the malleus is the largest of the auditory ossicles and the stapes the smallest, the relative volumes of these ossicles (= total volume of the ossicle—void space within the ossicle) do not always correlate directly with their sizes (see Table 1). Factors such as structural hollowness and the specific anatomical features of each ossicle can result in variations in volume that do not align with their overall dimensions. Consequently, it is important to correlate the geometrical dimensions of the ossicles and the porosity, as is done in this study.
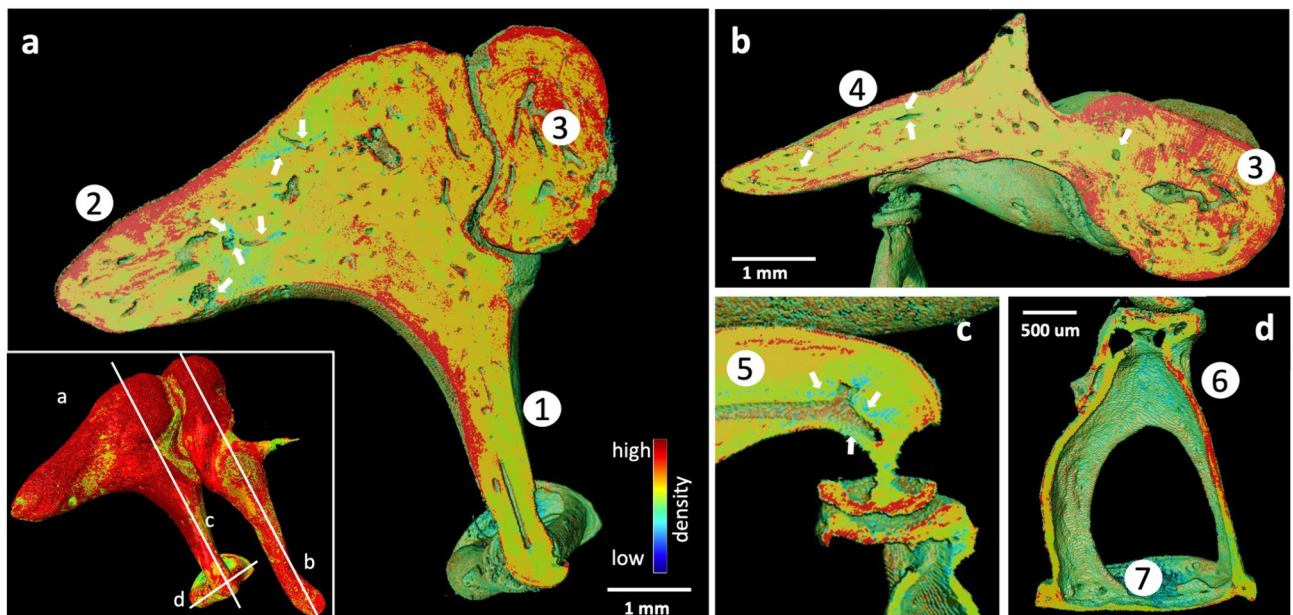

Figure 4. 3D volume rendering of sample 1 In (**a**) and (**b**), we can see that the short process of the incus (2), the malleus head (3), and the lateral region of the long process (1) show very high bone mineral density (red areas representing bone mineral density between 150 and 170). In contrast, several regions surrounding vessels appear relatively low in density, displayed in turquoise and indicated with little arrows in (**a**), (**b**), and (**c**). (**b**) Shows a virtual cut through the malleus, highlighting the ossicle's dense head (3) and lining. The manubrium (4) appears less dense than the rest of the malleus. The articular surface of the incudostapedial joint is displayed in (**c**), with low bone density surrounding vessels in the lenticular process (5). The red surfaces indicate high bone density. In (**d**), the stapes is shown. The anterior crus (6) in dark red represents very high bone density. The stapes footplate (7) is more orange with some red spots, indicating a medium–high bone density. Overall, the bone mineral density is high, as indicated in the surface rendering in the small window in (**a**).
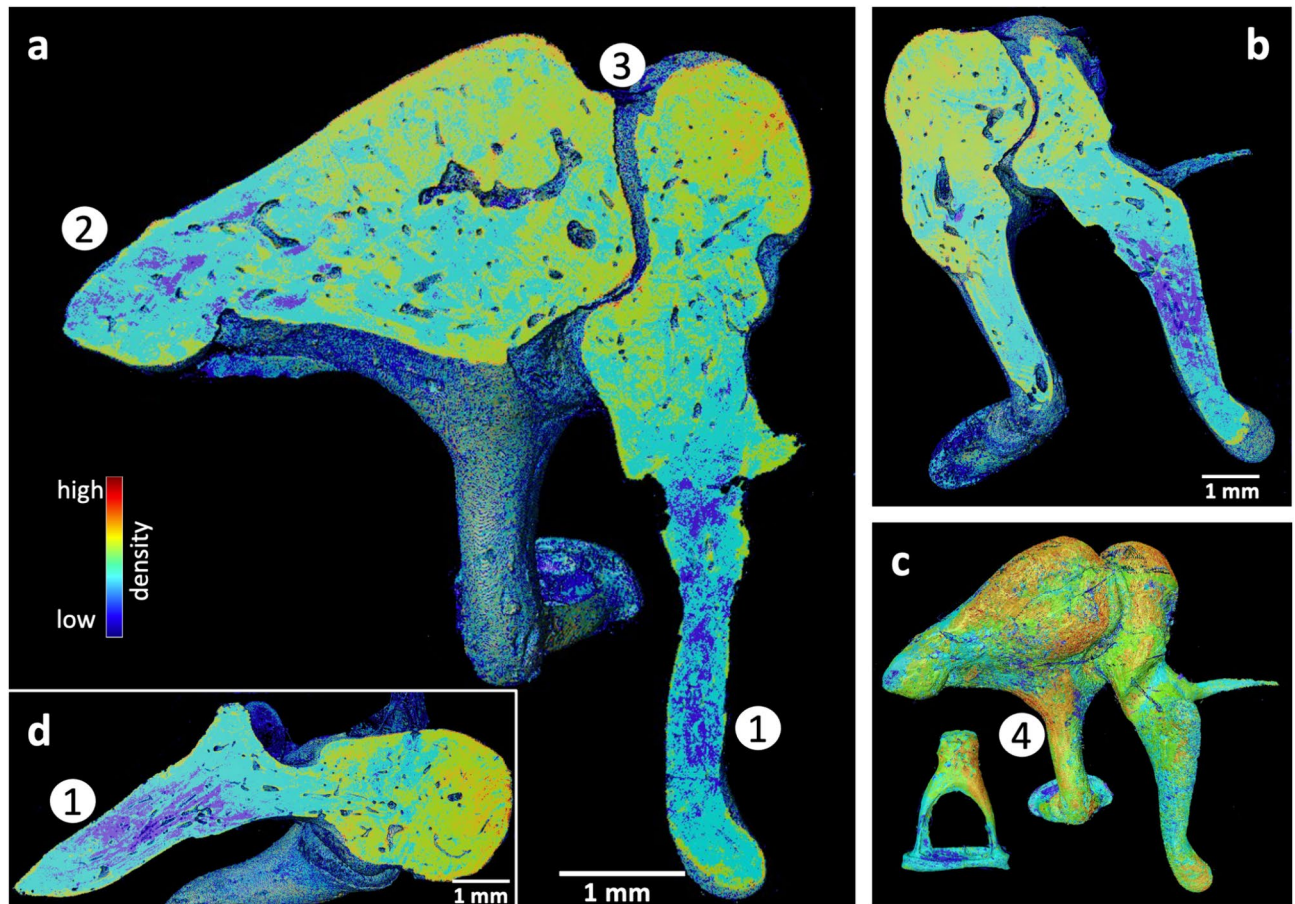
Figure 5. 3D volume rendering of sample 2. (**a**), (**b**), and (**d**) show the low bone mineral density in the manubrium (1) and in the short process (2) of the incus. Higher mineralized regions are visible in orange at the periphery of the malleus and the incus around their joint (IMJ) (3). The surface rendering in (**c**) highlights these higher mineralized areas in orange around the IMJ and, similar to sample 1, around the lateral part of the long process (4), the stapes head, parts of the footplate, and the anterior crus. In (**d**), the malleus is shown in a virtual sagittal cut, indicating the low-density area around the manubrium and the higher-density area towards the head. The rest of the ossicle bodies appear in a turquoise, representing a relatively low density in the range of 120–130.

The porosity of the auditory ossicles lies, on average, between 1.92 and 9.85%. In comparison, cortical bone has a porosity of 5–15%, whereas the porosity of trabecular bone ranges from 40 to 95%[25]. A lower degree of porosity was expected from the auditory ossicles, as they consist almost entirely of cortical bone, but no remodeling occurs.

Furthermore, we can note that areas with lower bone density correlate with areas with a higher degree of sponginess. In these areas, we also do not see any vascular channels. While we can define a vascular channel well in Sample 1 along the long process of the incus, this is not possible in Samples 2 and 3 (see Fig. 3). A possible explanation could be that the low or absent blood supply leads to these highly porous areas. Bone remodeling can only occur properly if the growth factors and nutrients reach a particular region. If the blood vessels cannot reach a particular area anymore, the remodeling process is disrupted, leading to the erosion of this area. Previous reports have stated that the long process of the incus is indeed the most susceptible area to bone erosion[26–29]. For the volume and porosity analysis, we segmented the ossicles first and performed the calculations based on the label fields. Accordingly, the segmentation accuracy determines the accuracy of the volume and porosity calculations. The isotropic voxel size of 2.75 μm is the highest level of detail reported so far to define the volume of human auditory ossicles. It determines the limit of differentiable grey levels and, therefore, the accuracy of the calculations. Hence, we are confident that we can discriminate bone from cavities well and that our values are reliable. Further, we found a difference in the overall bone density between Sample 1 and the other samples. However, the bone density distributions within the three analyzed samples show very similar patterns. Furthermore, we can not know how significant the differences would be if we looked at the absolute values for the bone densities. Therefore, we can not draw meaningful conclusions about the inter-sample variance. However, we believe that the similar pattern observed in all samples is more meaningful.

To our knowledge, Morris et al.[4] has been the only one who reported a bone density analysis for human samples. However, the samples were Thiel-fixed. Unger et al.[30] and McDougall et al.[31] reported degradation and fragmentation of cells and significant change in biomechanical properties of the tissue that underwent
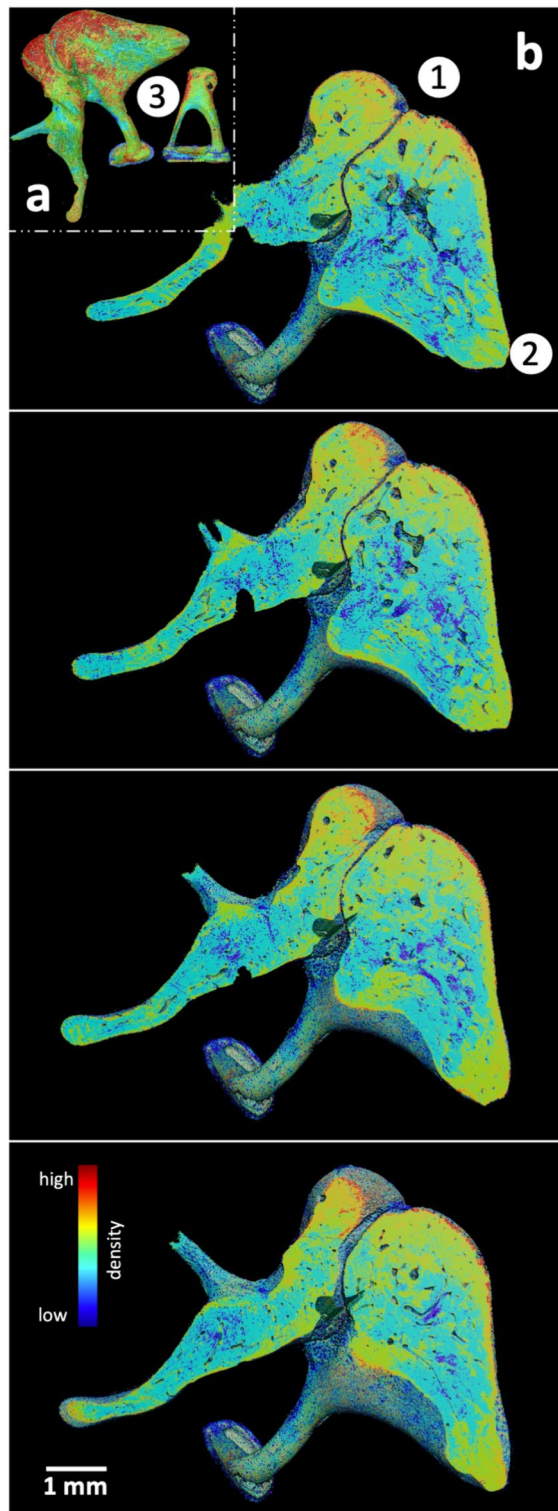
Figure 6. 3D volume rendering of sample 3. (**b**) Shows virtual transversal cuts from inferior to superior, revealing the high bone density areas at the periphery of the incudomalleolar joint (1) and the short process (2) of the incus. The malleus and incus body appear in turquoise and dark blue, indicating relatively low bone density in the range of 110–130. The surface rendering in (**a**) highlights the high-density areas around the incudomalleolar joint and the anterior crus of the stapes (3).
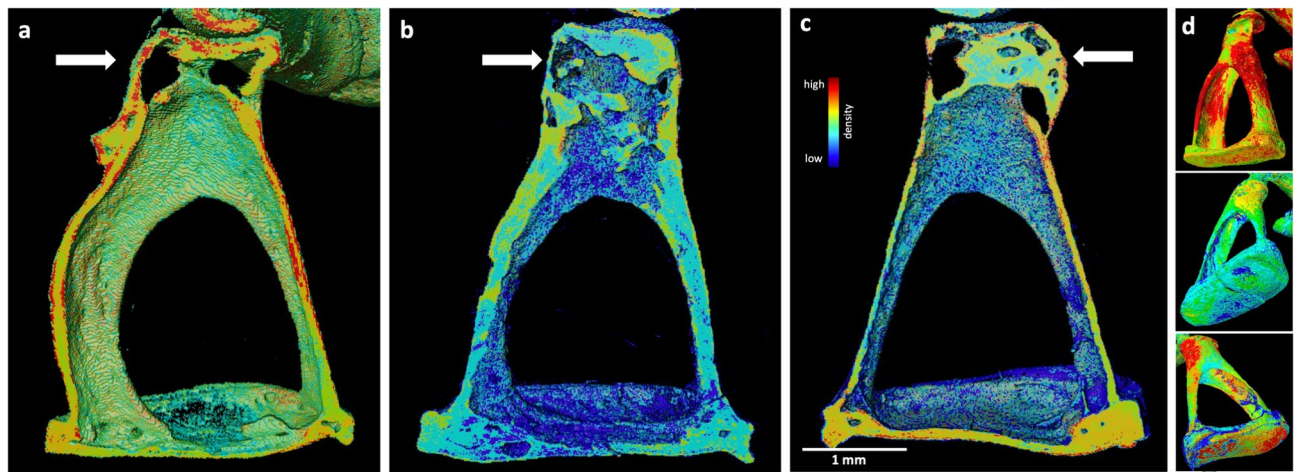
Figure 7. 3D volume rendering of the three stapedes. The attachment sites of the stapedius muscle at the neck of the stapedes are indicated with white arrows. The attachment site of sample 1 shows high bone mineral density, displayed in (**a**). In (**b**), we see stapes 2. The attachment site shows higher density than the rest of the stapes. Stapes 3 is shown in (**c**). The attachment site also shows high bone mineral density. (**d**) Displays the surface rendering of the three stapedes. The top image shows stapes 1, with highly dense crura and parts of the footplate. Stapes 2 is shown in the middle with higher mineralized spots on its footplate. The bottom image shows the surface rendering of stapes 3. Here, too, the footplate reveals highly dense spots.

Thiel-fixation. The Thiel-fixation could, therefore, affect bone mineralization as well. Nevertheless, Morris et al.[4] hypothesized that similar to long bone, bone remodeling in the auditory ossicles occurs where many biomechanical forces are applied. He, therefore, suggested that the incudomalleolar joint (IMJ), which facilitates just biaxial motion[32] and, therefore, is not exposed to many forces, should have a higher bone mineral density compared to the incudostapedial joint (ISJ), which allows multiaxial motion[33], and is therefore exposed to more forces. Our findings only partially support his hypothesis. The IMJ shows a relatively high bone density for sample 1. However, the ISJ of the same sample showed an even higher bone mineral density. For samples 2 and 3, we could also see that the IMJ is highly mineralized. However, we could not see any considerable differences compared to the ISJ. However, further findings are in line with his suggestions that less remodeling happens at sites of lower forces, which shows in higher mineralization patterns at the periphery of the malleus and the incus, around the incudomalleolar joint, and along the lateral side of the long process.

In addition, all samples showed high bone density spots at the stapes footplate, between 140 and 150 for sample 2 and up to 170 for sample 1 and 3. This agrees to some extent with Morris et al.[4], who stated that the stapes footplate is the densest part of the ossicular chain.

We also saw that the stapedius muscle's attachment site at the stapes' neck and the anterior crus show very high bone mineral density, as seen in Fig. 7. For sample 1, the attachment site shows the highest mineralization of the three samples, which aligns with the overall mineralization pattern of that sample. Sample 2 shows the lowest bone density at the attachment site. However, the overall density of stapes 2 is lower than the other two samples. Therefore, the area of the attachment site differentiates from the rest of the stapes, with a much higher density in the range of 140. Hill et al.[8], who investigated long bones, suggested that bone remodeling should not occur at sites of ligamentous attachment in order to provide stability. Thus, these sites should have higher bone mineralization. Therefore, our findings concerning the stapedius muscle's attachment site support the findings of Hill et al.[8].

In summary, we analyzed the bone density distribution in the ossicular chain of fresh-frozen human temporal bones for the first time. Bone density distribution plays a crucial role in the ossicles. It is essential for mass distribution, as the ossicles are suspended in an air-filled cavity. Therefore, the overall density also influences how well sound is transmitted. Our findings showed a higher density along the periphery of the ossicles, which may help to maintain mass balance. Further, we suggest that the high density of the stapes footplate ensures proper coupling to the oval window and, hence, proper sound transmission to the inner ear. In addition, we analyzed the volume and porosity of the ossicles. We found a negative correlation between holey areas within the ossicles and the density within that area. Further, we saw a similar high bone density pattern along areas exposed to lower forces, such as the periphery of the malleus and incus, along the IMJ, and the long process of the incus. In addition, the anterior crus and the parts of the stapes footplate also showed high bone density.

Limitations

For the bone density analysis, we did not scan a bone mineral density calibration phantom as it has been done previously, e.g., by Talon et al.[34]; therefore, we do not have absolute bone density values we can compare the three samples to. We described differences in bone density and density distribution based on a scale we defined as described in *Methods*. For that reason, we cannot draw conclusive results from the specific numerical values; we can only draw conclusions from the distribution patterns. Additionally, the analyzed samples were subjected to intense X-ray radiation, freezing, and thawing, which might have affected the bone composition. Consequently,

absolute values could have also been misleading. Therefore, we believe the reported comparative description is more meaningful than absolute values. In addition, fresh-frozen specimens were chosen for the experiments compared to fresh specimens because the following reasons had to be considered: One must apply for beamtime at least six months before the actual experiments can take place, and we cannot foresee when the experiments will take place and if there are fresh human temporal bones available at this time. In addition, it takes several hours to perform synchrotron-based microtomography scans (including the setup), and technical problems can arise that can delay the scan time. During this time, the human temporal bones would progress with their degradation.

Our study was constrained by the small sample size (N = 3). This is mainly due to the availability of human samples and the highly competitive allocation of beamtime at the SLS. Due to the limited sample size, a comprehensive statistical analysis was not feasible in our study. Therefore, our findings are not representative of all ossicles.

Moreover, to have an accurate comparison between the samples, bone density calibration measurements should have been performed for each sample separately. This would have accounted for variability in sample positioning and acquisition parameters (such as distance and absorption differences) that cause slight variations in the grayscale. Therefore, the gray levels between samples cannot be directly compared. Instead, we focus on comparing patterns rather than specific numerical values in arbitrary units.

Methods

Ethical issues

The study protocol was approved by the local ethical committee (Kantonale Ethikkommission Bern, KEK-BE 2016-00887) and the local ethical committee for the Paul Scherrer Institute (Ethikkommission Nordwest-und Zentralschweiz, 2017-00805). We received the temporal bones from body donors who gave written informed consent to conduct clinical research with the tissue. All methods were performed in accordance with the regulations and guidelines provided by the Declaration of Helsinki.

Sample preparation

Three fresh-frozen human temporal bones with no known history of middle ear diseases were analyzed. Regarding mechanical characteristics, fresh-frozen specimens are commonly used to study middle ear mechanics[35]. Two were left ears (Sample 1 and Sample 2), and Sample 3 was a right ear. To diminish the absorption of X-rays during the imaging, the area of interest had to be extracted from the temporal bone. The auditory system, from the external auditory canal, middle and inner ear to the internal auditory canal, was kept intact but skeletonized as much as possible. Laterally, the concha was removed, conserving the bony and cartilaginous external auditory canal. Posteriorly and superiorly, the air cells of the mastoid portion were removed until the tegmen tympani and the antrum. Inferiorly, the soft tissue was removed until the internal carotid artery, the jugular bulb, and the insertion of the Eustachian tube. Medially, the petrous part of the temporal bone was left intact. The surrounding bone was drilled to 1 mm remaining thickness to avoid absorption of the X-rays by the temporal bone. Finally, the sample had a size of approximately 5×2 cm^2. Each specimen was placed in a custom-made cylindrical holder (diameter of 25 mm) and mounted on the rotation stage at the TOMCAT beamline at the Swiss Light Source (Paul Scherrer Institute, Switzerland), as illustrated in Fig. 8. To prevent the samples from drying out during the acquisition, they were wrapped in neuro-patties soaked in a sterile saline solution, and the top of the holder was sealed with a plastic film.

Image acquisition and reconstruction

High-resolution (HR) static (3D) propagation-based phase-contrast images were acquired at the TOMCAT beamline at the Swiss Light Source (Paul Scherrer Institute, Switzerland). The setup consisted of the GigaFRoST camera[36] and a 4× magnification macroscope (4× White-Beam Macroscope, Optique Peter), giving an effective pixel size of 2.75 μm[37]. Polychromatic radiation (50% filtered white beam with an additional 4-mm glass filter) was used to optimize image quality. The exposure time was set to 1 ms and the propagation distance to 250 mm. Because the Field-of-View (FoV) of 5.5×5.5 mm^2 was not big enough to image the entire middle ear at once, several sub-scans were taken and stitched together after the reconstruction. For each sub-scan, 4000 images were collected over 360°, together with 50 darks and 100 flats, to correct for the camera's dark current and inhomogeneities from the X-ray beam, respectively. The number of sub-scans varied between 116 and 260 scans depending on the sample size. The datasets were reconstructed in absorption and in phase, i.e., using Paganin's single-distance phase retrieval method[38] before using the Gridrec algorithm[39] to reconstruct the tomograms. The parameters used to get the best contrast (i.e., the best delta/beta ratio) for the acquisitions were $\delta = 1e{-}7$, $\beta = 1e{-}9$ for a propagation distance of 250 mm. After the reconstruction, the sub-scans were stitched using NRStitcher[40] to obtain one 3D dataset containing the entire peripheral auditory system. Therefore, we ended up with one full dataset in absorption contrast and one in phase contrast mode for each sample.

The interaction of X-rays with matter leads to attenuation and refraction of the X-ray beam, which causes an amplitude reduction and a phase shift of the passing beam that is specific to the composition of the material the beam passes through. Accordingly, the image pixel value's intensity will differ between tissue compositions. The greater the difference between an image's minimum and maximum intensity value, the better the contrast. In a clinical X-ray, the contrast between tissues of similar composition is very low because we only consider the difference in absorption coefficient (attenuation-based X-ray imaging). We can, therefore, distinguish bone from air well but not so well between soft tissues. However, in phase-contrast imaging, we also elaborate on refraction-based imaging, which improves soft-tissue contrast by probing the phase shift induced by the individual tissues as illustrated in Fig. 9. This phase shift is usually much bigger than the difference in the attenuation coefficient
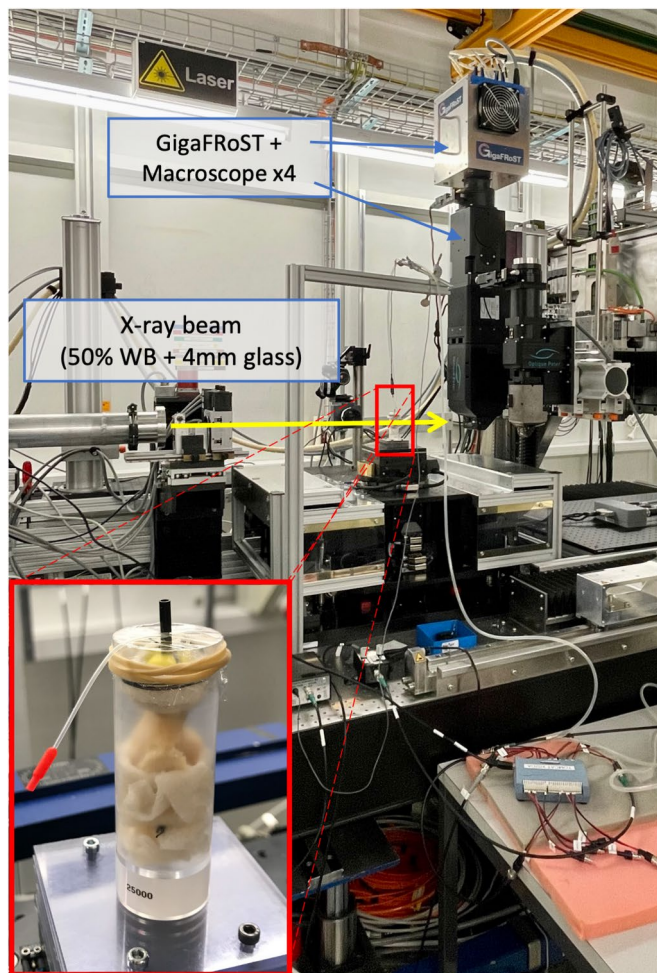
Figure 8. Experimental setup at the TOMCAT beamline of the Swiss Light Source (Paul Scherrer Institute, Switzerland). The sample is shown in the zoom-in window. It is fixed in a custom-made cylindrical sample holder and screwed onto the rotation stage. Saline-soaked neuro-patties are wrapped around it, and the top is sealed with a plastic film to prevent the sample from drying out.

for soft tissue. The datasets reconstructed in phase contrast were, therefore, used for the bone density distribution analysis. The better contrast helped us to differentiate between the fine differences in bone density.

To define the edges for the volume and porosity analysis at utmost precision, the reconstructions in absorption contrast was used. This allowed for a more accurate volume calculation, as the single-distance phase retrieval method entails a low-pass filter, which is known to enhance the contrast but blur the edges of the structures.

The native projection of all data sets is 32 bits. However, we reconstructed all data sets in 8 bits to limit the data size. The same minimum and maximum grayscale range were used for the absorption and phase contrast data sets, respectively.

Quantification and descriptive analysis

The commercial Amira-Avizo software (Thermo Scientific Co., version 2020.3.1) with the XImagePAQ— Advanced Image processing and quantification extension was used for the 3D visualizations and the analysis of all samples. For the volume and porosity analysis, an integrated watershed algorithm[41] was used to segment the three ossicles from each other within the ossicular chain. Before the analysis, we cropped the images to the middle ear, the area of interest, to reduce the size and computational effort. We then performed the volume analysis with a built-in function in Amira, which sums all the voxels represented in the label fields obtained from the watershed segmentation. The label field included only the bone material and not the void spaces. The same label fields were used for the porosity analysis. We obtained the porosity value with another module provided by the Amira software called *ASMR Porosity*. The module defines porosity as the percentage of void spaces within a material, calculated as the ratio of the volume of voids to the total volume. It measures porosity on a slice-by-slice basis and detects only void spaces enclosed by solid material. This means that all cavities, including vascular channels, are included in the porosity measurement.
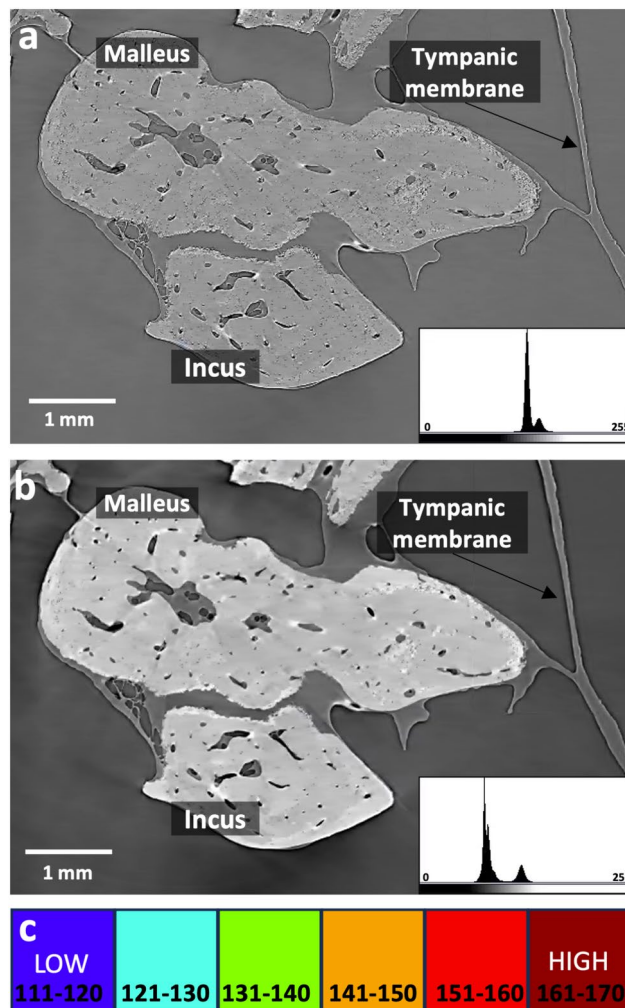
Figure 9. 3D tomographic dataset of an incudomalleolar joint reconstructed in absorption (**a**) and in phase-contrast (**b**). Paganin's phase retrieval method enhances the contrast, which makes soft tissue structure better visible and lets us distinguish different degrees of bone density within the ossicle. We can see this difference in the greyscale bar and the corresponding histogram in the right bottom corner of (**a**) and (**b**). However, the edges in the image reconstructed in absorption (**a**) are sharper, which allows a more accurate volume calculation. In (**c**), the scale we defined is shown with the color representing each group. From dark blue, representing the lowest bone density range of 111–120, to dark red, representing the highest bone density range of 161–170.

We used the reconstructed datasets in phase contrast for the bone density distribution analysis. Because we did not scan a bone density calibration phantom, we first performed a min–max normalization on all the data sets to obtain normalized gray values between 0 and 1. The voxel value for air varied between the samples but was always the minimum. After the normalization, the value for air was set to 0 for every dataset. To get a scale similar to the Hounsfield Unit (HU), which allows us to compare the bone densities between different samples, we arbitrarily assigned the normalized voxel value of the perilymph for every sample to 100. We then had two defined values (air = 0 and perilymph = 100) to calculate values for the densities based on a linear transformation and the normalized voxel values of the individual sample. This new scale gave us bone density values between 110 and 170. The higher the number, the denser the bone. We linearly split the scale into six groups and assigned a color for each group to differentiate between different degrees of bone density mineralization. In the segmentation editor of the Amira software, we assigned these color groups to the appropriate voxel values and segmented the ossicular chain based on these different bone density groups. The defined color range goes from dark blue, representing the least dense, to dark red, representing the most dense areas, as shown in 9c.

The Amira-Avizo's built-in module used to calculate the porosity cannot differentiate between porous bone and other cavities and, therefore, includes all the void spaces surrounded by solids, i.e., lacunae, blood vessels, and other bone spaces like a crack.

Data availability
Due to the large size of the presented datasets, data will remain stored by the PSI Research Infrastructure following PSI Data Policy (https://www.psi.ch/en/science/psi-data-policy). Full accessibility without restrictions

will be granted upon request via email to the corresponding Author, including remote access functionality. For simplicity, we have changed the naming of the samples in this article. Sample 1 corresponds to the raw data of Fresh1, Sample 2 corresponds to the raw data of Fresh6, and Sample 3 corresponds to the raw data of Fresh3.

References

1. Békésy, G. V. *Experiments in hearing* (Mcgraw Hill, 1960).
2. Delsmann, M. M. *et al.* Prevention of hypomineralization in auditory ossicles of vitamin d receptor (vdr) deficient mice. *Front. Endocrinol.* https://doi.org/10.3389/fendo.2022.901265 (2022).
3. Kuroda, Y. *et al.* Hypermineralization of hearing-related bones by a specific osteoblast subtype. *J. Bone Miner. Res.* **36**, 1535–1547. https://doi.org/10.1002/jbmr.4320 (2021).
4. Morris, C., Kramer, B. & Hutchinson, E. F. Bone mineral density of human ear ossicles: An assessment of structure in relation to function. *Clin. Anat.* **31**, 1158–1166. https://doi.org/10.1002/ca.23231 (2018).
5. Rolvien, T. *et al.* Early bone tissue aging in human auditory ossicles is accompanied by excessive hypermineralization, osteocyte death and micropetrosis. *Sci. Rep.* https://doi.org/10.1038/s41598-018-19803-2 (2018).
6. Anschuetz, L. *et al.* Synchrotron radiation imaging revealing the sub-micron structure of the auditory ossicles. *Hear. Res.* **383**, 107806. https://doi.org/10.1016/j.heares.2019.107806 (2019).
7. Ilusmedical. Anatomía del oido (2024).
8. Hill, P. Bone remodelling. *Br. J. Orthod.* **25**, 101–107 (1998).
9. Kanzaki, S. *et al.* Impaired vibration of auditory ossicles in osteopetrotic mice. *Am. J. Pathol.* **178**, 1270–1278. https://doi.org/10.1016/j.ajpath.2010.11.063 (2011).
10. Swinnen, F. K. *et al.* Association between bone mineral density and hearing loss in osteogenesis imperfecta. *Laryngoscope* **122**, 401–408. https://doi.org/10.1002/lary.22408 (2012).
11. Marotti, G., Farneti, D., Remaggi, F. & Tartari, F. Morphometric investigation on osteocytes in human auditory ossicles. *Annals Anat.* **180**, 449–453. https://doi.org/10.1016/S0940-9602(98)80106-4 (1998).
12. Schaffler, M. B. & Kennedy, O. D. Osteocyte signaling in bone. *Curr. Osteoporos. Rep.* **10**, 118–125. https://doi.org/10.1007/s11914-012-0105-4 (2012).
13. Buccino, F. *et al.* Assessing the intimate mechanobiological link between human bone micro-scale trabecular architecture and micro-damages. *Eng. Fract. Mech.* **270**, 108582. https://doi.org/10.1016/j.engfracmech.2022.108582 (2022).
14. Buccino, F. *et al.* Osteoporosis and covid-19: Detected similarities in bone lacunar-level alterations via combined ai and advanced synchrotron testing. *Mater. Des.* **231**, 112087. https://doi.org/10.1016/j.matdes.2023.112087 (2023).
15. Decraemer, W. F., Dirckx, J. J. & Funnell, W. R. Three-dimensional modelling of the middle-ear ossicular chain using a commercial high-resolution X-ray ct scanner. *JARO J. Assoc. for Res. Otolaryngol.* **4**, 250–263. https://doi.org/10.1007/s10162-002-3030-x (2003).
16. Kaftan, H. & Böhme, M. Geometric parameters of the ossicular chain as a function of its integrity: A micro-ct study in human temporal bones (2015).
17. Greef, D. D. *et al.* Details of human middle ear morphology based on micro-ct imaging of phosphotungstic acid stained samples. *J. Morphol.* **276**, 1025–1046. https://doi.org/10.1002/jmor.20392 (2015).
18. Mikhael, C. S., Robert, W., Funnell, J. & Bance, M. Middle-ear finite-element modelling with realistic geometry and a priori material-property estimates (2005).
19. Nager, G. T., Nager, M. & Baltimore, M. Annals of otology, rhinology (2015).
20. Hamberger, C.-A. & Wevsall, J. *Vascular supply of the tympanic membrane and the ossicular chain* https://doi.org/10.3109/00016486409134581 (1964).
21. Anson, B. J. & Winch, T. R. Vascular channels in the auditory ossicles in man (1974).
22. Gulya A.J. *Anatomy of the Temporal Bone with Surgical Implications* (Parthenon Pub. Group, 1995).
23. Péus, D., Dobrev, I., Pfiffner, F. & Sim, J. H. Comparison of sheep and human middle-ear ossicles: anatomy and inertial properties. *J. Comp Physiol. A Neuroethol. Sensory Neural Behav. Physiol.* **206**, 683–700. https://doi.org/10.1007/s00359-020-01430-w (2020).
24. Manoharan, S. M., Gray, R., Hamilton, J. & Mason, M. J. Internal vascular channel architecture in human auditory ossicles. *J. Anat.* **241**, 245–258. https://doi.org/10.1111/joa.13661 (2022).
25. Morgan, E. F., Unnikrisnan, G. U. & Hussein, A. I. Bone mechanical properties in healthy and diseased states. *Annu. Rev. Biomed. Eng.* https://doi.org/10.1146/annurev-bioeng-062117 (2018).
26. Hamberger, C. A., Marcuson, G. & Wersäll, J. Blood vessels of the ossicular chain. *Acta Oto-Laryngologica* **56**, 66–70. https://doi.org/10.3109/00016486309138753 (1963).
27. Bast, T. H. & Anson, B. Development of the incus of the human earl illustrated in atlas series 2 (1959).
28. Gerlinger, I. *et al.* Necrosis of the long process of the incus following stapes surgery: New anatomical observations. *Laryngoscope* **119**, 721–726. https://doi.org/10.1002/lary.20166 (2009).
29. Lindeman, H. Some histological examinations of the incus and stapes with especial regard to their vascularization. *Acta Oto-Laryngologica* **57**, 319–326. https://doi.org/10.3109/00016486409134582 (1964).
30. Unger, S., Blauth, M. & Schmoelz, W. Effects of three different preservation methods on the mechanical properties of human and bovine cortical bone. *Bone* **47**, 1048–1053. https://doi.org/10.1016/j.bone.2010.08.012 (2010).
31. McDougall, S., Soames, R. & Felts, P. Thiel embalming: Quantifying histological changes in skeletal muscle and tendon and investigating the role of boric acid. *Clin. Anat.* **33**, 696–704. https://doi.org/10.1002/ca.23491 (2020).
32. Sim, J. H. & Puria, S. Soft tissue morphometry of the malleus-incus complex from micro-ct imaging. *JARO J. Assoc. for Res. Otolaryngol.* **9**, 5–21. https://doi.org/10.1007/s10162-007-0103-x (2008).
33. Drake, R. & Vogl, M. A. *Gray's Anatomy for Students* 15th edn. (Elsevier, 2015).
34. Talon, E., Visini, M., Wagner, F., Caversaccio, M. & Wimmer, W. Quantitative analysis of temporal bone density and thickness for robotic ear surgery. *Front. Surg.* https://doi.org/10.3389/fsurg.2021.740008 (2021).
35. Graf, L. *et al.* Effect of conservation method on ear mechanics for the same specimen. *Hear. Res.* **401**, 108152. https://doi.org/10.1016/j.heares.2020.108152 (2021).
36. Mokso, R. *et al.* Gigafrost: The gigabit fast readout system for tomography. *J. Synchrotron Radiat.* **24**, 1250–1259. https://doi.org/10.1107/S1600577517013522 (2017).
37. Bührer, M. *et al.* High-numerical-aperture macroscope optics for time-resolved experiments. *J. Synchrotron Radiat.* **26**, 1161–1172. https://doi.org/10.1107/S1600577519004119 (2019).
38. Paganin, D., Mayo, S., Gureyev, T., Miller, P. & Wilkins, S. Simultaneous phase and amplitude extraction from a single defocused image of a homogeneous object (2002).
39. Marone, F. & Stampanoni, M. Regridding reconstruction algorithm for real-time tomographic imaging. *J. Synchrotron Radiat.* **19**, 1029–1037. https://doi.org/10.1107/S0909049512032864 (2012).

40. Miettinen, A., Oikonomidis, I. V., Bonnin, A. & Stampanoni, M. Nrstitcher: Non-rigid stitching of terapixel-scale volumetric images. *Bioinformatics* **35**, 5290–5297. https://doi.org/10.1093/bioinformatics/btz423 (2019).
41. Serra, J. Image analysis and mathematical morphology. *Biometrics* **39**, 536–537 (1983).

Acknowledgements

Author contributions

A.I., M.Sc., A.B, W.W, L.A. conceived the experiments, A.I., M.Sc, A.B., L.A. conducted the experiments, L.A. dissected and prepared the samples, A.I. reconstructed the data, A.I. and F.S. analyzed the results, A.I. created the figures and wrote the original draft, L.A., W.W., A.B., M.Sc., provided constructive suggestions for results and discussion, M.C. and M.St. provided administrative support and resources. All authors reviewed and approved the manuscript.

Competing interests

The authors declare no competing interests.

Additional information

Correspondence and requests for materials should be addressed to A.I.

Reprints and permissions information is available at www.nature.com/reprints.

Publisher's note Springer Nature remains neutral with regard to jurisdictional claims in published maps and institutional affiliations.